Lab on a Chip

Accepted Manuscript

This is an *Accepted Manuscript*, which has been through the Royal Society of Chemistry peer review process and has been accepted for publication.

Accepted Manuscripts are published online shortly after acceptance, before technical editing, formatting and proof reading. Using this free service, authors can make their results available to the community, in citable form, before we publish the edited article. We will replace this *Accepted Manuscript* with the edited and formatted *Advance Article* as soon as it is available.

You can find more information about *Accepted Manuscripts* in the **Information for Authors**.

Please note that technical editing may introduce minor changes to the text and/or graphics, which may alter content. The journal's standard **Terms & Conditions** and the **Ethical guidelines** still apply. In no event shall the Royal Society of Chemistry be held responsible for any errors or omissions in this *Accepted Manuscript* or any consequences arising from the use of any information it contains.

Lab On A Chip

PAPER

Insect-Human Hybrid Eye (IHHE): An Adaptive Optofluidic Lens Combining Structural Characteristics of Insect and Human Eyes

K. Wei, H. Zeng and Y. Zhao[a*],

Insect compound eye and human camera eye are two exquisite optical systems created by the nature. The compound eye boasts an angle of view (AOV) up to 180º thanks to its hemispherical arrangement of hundreds of prime microscale lenses. The camera eye, on the other hand, can change shape to focus on objects at various depths yet accept light within a smaller AOV. Imitation of either imaging system has abounded but with limited success. Here, we describe a reconfigurable polymeric optofluidic device that combines architectural merits of both visions featuring a large AOV (up to 120º) with adaptive focusing capability (from 0 to 275 diopter (D)). This device consists of bi-layered microfluidics: an array of millimeter-sized fluidic lenses is integrated into the top layer and arranged on an elastomeric membrane embedded within the bottom layer. The membrane can be deformed from a planar surface into a series of dome geometries, rearranging individual fluidic lenses in desired curvilinear layouts. Meanwhile, each fluidic lens can vary its radius of curvature for monocular depth sensation. Such design presents a new perspective of tunable optofluidics for a broad range of applications, such as robotic vision and medical laparoendoscopy where adaptive focalization with a large viewing angle is at a premium.

Introduction

A plethora of daylight insects excel in observing the surrounding environment panoramically[1]. Investigations into their visual organs reveal a compound-eye mechanism, *e.g.* the eye of drosophila melanogaster contains up to 800 microscale ommatidia packed on a hemispherical surface with each facing towards a different orientation (from 0º to 180º)[2, 3]. Individual ommatidium manages both focusing (with a fixed focusing power about 4.7×10^4 diopter (D))[4] and imaging. The panoramic vision is created by integrating discrete views from every ommatidium in a pixelated fashion[1]. The notably wide angle of view (AOV) of the insect compound eye has precipitated many to engineer artificial counterparts owing to its potential use in consumer optics, medical endoscopy, robotic vision and other surveillance devices[5-7]. Three types of optical configurations are reported in recent demonstrations of artificial compound eye [8-23]. In the first type, a solid microlens array is arranged on a flat substrate and forms images through a pinhole array placed in the back focal plane. A deliberate pitch offset is introduced between the lens and the pinhole in order to tilt the direction of view and thus enlarge the overall AOV[8]. The second type closely resembles the configuration of insect compound eye[9, 12-15, 17]. Microlenses with fixed focusing powers are arranged on a hemispherical polymer dome and connected to either UV-written waveguides or flexible photoreceptors. The overall AOV of this configuration is determined by the number of the microlenses and their distribution. However, fabricating and assembling hundreds or thousands of microlenses with individually aligned photoreceptors on a convex substrate are not only technically challenging, but also demand substantial labor and cost. The third type is similar to the second type except for that the microlenses are replaced by diamond-machined microprisms. Each microprism steers incident light rays at different angles onto a 2D focal plane for image formation[11].

In natural and artificial compound eyes, the use of an array of lenslets increases the overall AOV yet at the sacrifice of the imaging performance[4, 24]. Due to the limited size of compound eyes, the aperture of each lenslet is only a few hundred μm or smaller. Such small aperture limits the amount of light that travels through the lenslet and leads to poor image quality especially in low illumination environment. Besides, each lenslet in the compound eye has a fixed focusing power and thus can best focus on objects within a certain range of distance. Although the small aperture ensures a fairly large depth of field, objects at different depths cannot be readily distinguished. Fortunately, nature offers another vision mechanism, *i.e.* human camera eye, which possesses a relatively large aperture and tunable focusing power. Despite a limited AOV due to the small total eye number, a human

camera eye enables a better image resolution and accommodation to detect monocular depth cues[25, 26] compared to the insect compound eye. Given these, it is plausible to expect that an optical component incorporating the characteristic features of both insect compound eye and human camera eye may offer a large AOV, good image quality, as well as vari-focal capability simultaneously for practical imaging/illumination applications.

Optofluidic devices that embed reconfigurable solid[27] or liquid[28, 29] optical elements within microfluidics are well known for its robustness in manipulating light propagation at micro/millimeter scale[30, 31], and may therefore be well suited for the integration of the two vision mechanisms. Of particular interest are the adaptive optofluidic lenses which have proven success in tuning the focusing power [32]. The in-plane adaptive focusing is often achieved by changing the radius of curvature of the liquid-liquid[33] or air-liquid interface[34], tuning the refractive index (RI)[35] or the RI profile[36] of mixing fluids, or plasmonics[37]. The out-of-plane adaptive focusing takes advantage of the adjustable surface tension within meniscus[38, 39], or the deformability of elastomeric membrane[40, 41].

In this study, we introduce a bio-inspired insect-human hybrid eye (IHHE) design that is implemented on an elastomeric optofluidic chip with out-of-plane adaptive focusing capability. The device consists of a bi-layered microfluidics: the top layer mimics the adaptive focusing capability of human camera eyes and the bottom layer can be reconfigured into various curvilinear layouts to mimic the hemispherical dome-shape in insect compound eye. The IHHE prototype delivers a viewing angle up to about 120° with the focusing power ranging from about 0D to 275D. The enhanced imaging performance, compact design and ease of operation provide a new avenue of adaptive optics for various applications.

Principle and design

The IHHE incorporates architectural merits of both insect apposition compound eye and human camera eye (Fig. 1a). A transparent polymeric big membrane that can be deformed from a planar surface into a spherical cap with varied radii of curvature is employed to mimic the dome-shape architecture of insect compound eye. An array (3×3) of single lenses is positioned on the big membrane, where the peripheral single lenses orient outwards when the big membrane deforms (Fig. 1b). Each single lens consists of a small transparent polymeric membrane and a fluid body underneath. The focusing power of a single lens can be adjusted by altering the fluid volume, so as to achieve accommodation function. A bi-layered microfluidic channel network provides fluid connections for deforming the big membrane and the small membranes of single lenses independently.

Simultaneous actuation of the big membrane and the small membranes yields a large overall AOV (Fig. 1c). When the big membrane remains un-deformed, the overall AOV is primarily determined by the focusing power of individual single lenses, and can be slightly enlarged by increasing the focusing power yet at the expense of increased optical aberration in each single lens. This is owing to the parabolic surface profile of the small membrane at large deflections[42]. To overcome this deficit, the big membrane is deformed into a spherical cap with a certain
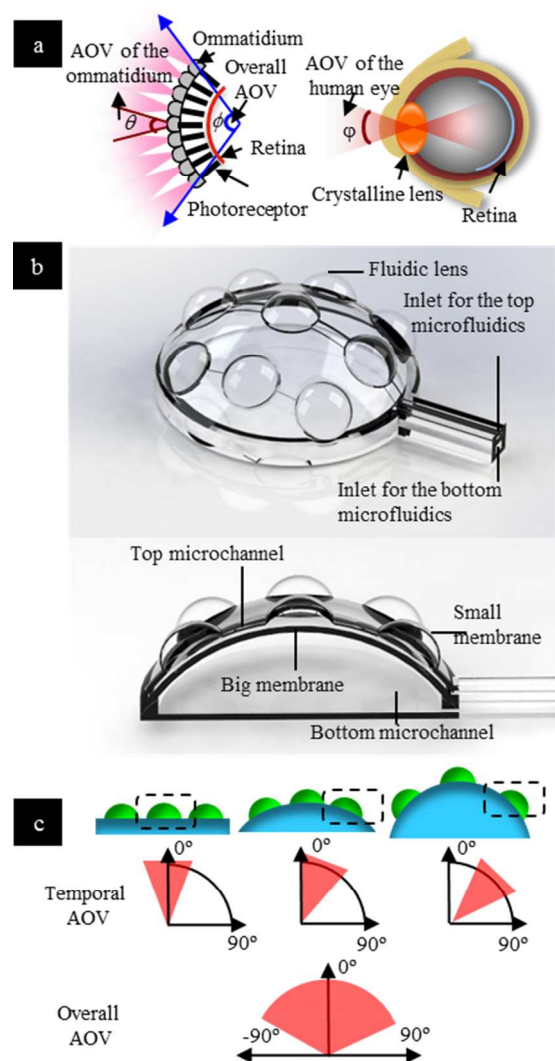

Fig. 1 Working principle of the IHHE. (a) Structures of insect apposition compound eye (left) and human camera eye (right). (b) IHHE combining architectural characteristics of the two vision systems by distributing an array of membrane-enveloped fluidic lenses on a big deformable membrane. (c) During operation, the big membrane forms a dome shape, which changes the AOV of the peripheral single lenses and thus increases the overall AOV. The focusing power of each single lens is tunable, allowing depth sensation along different orientations.

deflection, allowing the single lenses in the peripheral region to shift their optical axes outwards and capture images at a different viewing perspective. The tilted single lenses thus allow observation of the field at a different angle without inducing a large deflection in the small membranes. In the meantime each single lens can adjust its focusing power to compensate the object distance change due to the deformation of the big membrane and obtain a clear image with depth information. The overall AOV is obtained by combining the temporal AOVs of the peripheral single lenses during the entire actuation process and that of the single lens in the center. The AOVs obtained at different time points are slightly overlapped so that the temporally integrated overall AOV encompasses information of the entire field. Such usage of the deformable big membrane for temporal image integration avoids the fabrication of a large number of single lenses on a curved substrate. Tunable single lenses ensure proper focusing on all

the objects at different depths in the entire field. A schematic (perspective and cross-sectional side views) of the IHHE device is illustrated in Fig. 2a. The device contains a bi-layered polydimethylsiloxane (PDMS) substrate and a glass substrate. The bottom layer of the substrate is comprised of a circular big membrane (thickness: 200 μm; diameter: 10 mm) and a microchannel (height: 500 μm; width: 200 μm). The top layer of the substrate immediately above the bottom layer consists of nine circular small membranes (thickness: 50 μm; diameter: 2 mm; center-to-center distance: 2.5 mm), and three microchannels (height: 100 μm; width: 100 μm). The small membrane in the center of the array is concentric to the big membrane. The three microchannels connect the nine membranes to one fluidic inlet. The bottom surface of the PDMS substrate is attached to the glass substrate (thickness: 1 mm). The membrane deformation upon actuation was examined using finite element analysis (COMSOL Multiphysics 4.3b). In this analysis, the Young's modulus, density, and Poisson's ratio of the PDMS substrates were set at 1.8 MPa, 965 kg/m^3, and 0.49, respectively. In all cases, the small membrane of the single lens in the center had a deflection of about 0.2 mm. Fig. 2b shows that the maximal center deflection of the big membrane from 0 mm to about 3.0 mm can successfully tilt the optical axis of the peripheral lens from 0° to 45°. It also showed that the peripheral lenses maintained an essentially symmetric profile under all conditions.
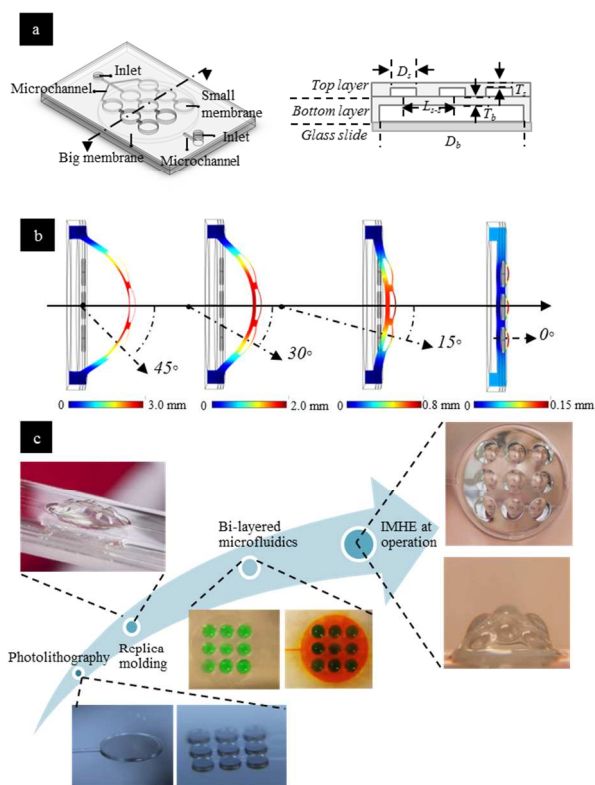
Fig. 2 Design, fabrication and assembly of the IHHE. (a) Schematic of the IHHE. D_s (diameter of the small membrane) = 2 mm; T_s (thickness of the small membrane) = 50mm; L_{s-s} (center to center distance between adjacent small membranes) = 2.5 mm; D_b (diameter of the big membrane) = 10 mm, T_b (thickness of the big membrane) = 200mm. (b) Simulated deformation profiles of the IHHE. (c) Left to right: master templates for the membranes; assembled IHHE; the bi-layered microfluidic network; and the top and side views of the IHHE while both the big membrane and the small membranes are deformed.

Fabrication and assembly

Fig. 2c illustrates the fabrication and assembly process. A cylindrical structure made of SU-8 2100 (Microchem, MA) (500 μm in thickness and 10 mm in diameter) served as the master template of the bottom microfluidic layer. The master template of the top microfluidic layer was fabricated using a double-layered photolithography process with SU-8 2050 (Microchem, MA), where nine cylindrical structures for molding the small membranes were 200 μm thick and the structures for molding the microfluidic channels were 100 μm thick. PDMS (Sylgard 184, Dow Corning, MI) was prepared by mixing the base and the curing agent at the weight ratio of 10:1 and degassed in a vacuum desiccator. It was cast onto the master templates of the top and the bottom layers, where polyester spacers were placed between the master template and a microscopic glass slide to control the membrane thickness. The glass was spun-coated with a 1.5 μm thick S1813 (Shipley) to assist peeling. After thermal curing, the bottom and top layers were aligned and plasma bonded to form the bi-layered PDMS substrate. The bottom layer was plasma treated and bonded to a glass substrate with RI of 1.5. After each bonding process, the PDMS substrate was heated on a hotplate for 30 min at 65°C to enhance the bonding. The optical medium with RI~1.41 (matching that of PDMS) was prepared by mixing 99% glycerol and deionized (DI) water at a weight ratio of 3:2. The medium was filled into the microfluidic channels in both layers by a syringe pump (Pump 11 Elite, Harvard Apparatus, MA) at the flow rate of 20ml/hr. For visualization purpose, the microfluidic network in the top layer of an assembled device was filled with green food color; and that in the bottom with yellow food color. The top and side view images of the IHHE prototype were captured while both the big membrane and the small membranes were deformed.

Results

Tunable focusing power

Because the RI of the optical medium matches that of PDMS, the effective focusing power (P_{lens}, the reciprocal of effective focal length) of each membrane-enveloped fluid lens is determined primarily by the focusing power at the air-PDMS surface. It was measured by a custom-built fluorescence ray tracing system that consisted of a laser diode (diameter: 2 mm; wavelength: 532 nm), the IHHE prototype, a glass trough (length: 120 mm) filled with the deionized water containing Rhodamine fluorescence dye (Sigma Aldrich, MO; RI=1.33) and a charge-coupled device (CCD) camera (Casio EX-F1). During the entire measurement, the big membrane was kept planar. A collimated beam ray from a green laser was incident on one single lens in the IHHE prototype and converged. The fluorescence image showing the optical path was analyzed by ImageJ (version 1.47, NIH) to calculate the distance (v) between backside of the glass substrate and the focal point in the medium. To determine P_{lens}, the measuring system was simplified as an equivalent air system (as illustrated in Fig. 3a) where the light travelled through three interfaces sequentially, namely: the air-PDMS interface, the PDMS-glass interface and the glass-fluorescence interface. P_{lens} was determined by applying the vergence equation at each interface:

$$P_{lens} = \frac{1000}{\dfrac{v}{1.33} + \dfrac{s+t}{1.4} + 0.67}$$ (1)

where s is the center deflection of the small membrane; and t is the total thickness of the bi-layered PDMS substrate (0.95 mm in this study).
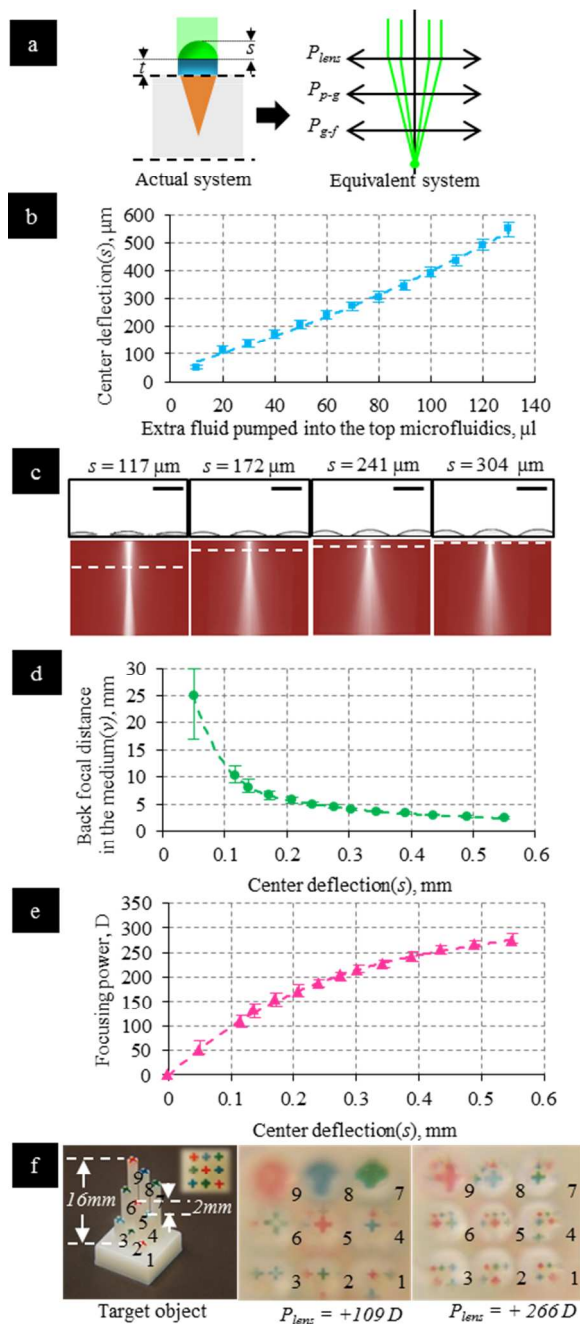

Fig. 3 Focusing power measurement while the big membrane was undeformed. (a) Ray tracing schematic and its equivalent air model. (b) Center deflection of the small membrane as a function of fluid addition into the microfluidic channel in the top layer. (c) Representative images of beam convergence in the fluorescence medium at s = 117 μm, 172 μm, 241 μm and 304 μm, respectively. Scale bars denote 2mm. (d) Back focal distance in the medium as a function of the center deflection of the small membrane. (e) The focusing power of the single lenses. (f) Demonstration of adaptive focusing by viewing an array of pillars whose top surfaces were placed at different depths.

The center deflection of the lens was measured by a goniometer (ramé-hart, Model 200, NJ). Extra optical medium of 10 to 130 μl was supplied to the top microfluidic channels at an increment of 10 μl. The results showed the center deflection of the small membrane increased with increasing fluid volume, from about 50 μm at 10 μl to about 550 μm at 130 μl (Fig. 3b). The focal point also changed with the small membrane deflection, as evidenced by ray tracing results (Fig. 3c). The corresponding back focal distance in the medium decreased from about 25.0 mm at the center deflection of 50 μm to about 2.5 mm at the center deflection of 550 μm (Fig. 3d). Calculation showed that P_{lens} varied from 0D at the planar surface to 275D at the maximal center deflection of 550 μm (Fig. 3e). This was well beyond the range of the focusing power of a normal human camera eye, which ranges from 16.3D to 23.0D. To demonstrate the adaptive focusing capability, the IHHE prototype was used to examine a 3×3 array of pillars (Fig. 3f). All the pillars were 2 mm in diameter, and spaced by 2.5 mm from the neighbors. Each pillar had a different length, from 2 mm to 18 mm with an increment of 2 mm. For better visualization, a crossing cut was created on the top surface of each pillar and stained by food color. The bottom substrate of the pillar array was positioned at 40 mm from the IHHE. The pillars and the bottom substrate were fabricated using a 3D printer (Objet 24, Stratasys, MN). The images viewed through the membrane lenses array were obtained while changing the focusing power of the single lenses from 109D to 266D. At 109D, pillars #1 through #6 (where the distance from the lens to the pillar top varied from 38 mm to 28 mm) were clearly viewed through lens #1 through #6, whereas pillar #7 through #9 were somewhat defocused. When the focusing power increased to 266D, images of pillars #7 through #9 came into focus, whereas those of pillars #1 through #6 became blurry.

Tunable AOV

Dome-shaped geometries of the deformed big membrane at different deflections were examined (Fig. 4a). Extra fluid from 240 to 640 μl was pumped into the bottom microfluidic network at the increment of 40 μl. Results showed that the center deflection of the big membrane (h) increased
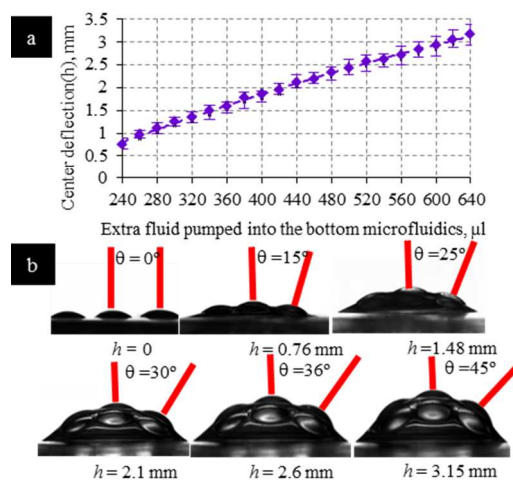

Fig. 4 Tunable AOV. (a) Center deflection of the big membrane changes with the volume of extra fluid supplied into the microfluidic channel in the bottom layer. (b) Orientation of the center lens and a peripheral single lens in the middle row while the big membrane was at different center deflections. Red line: the optical axis of single lens.
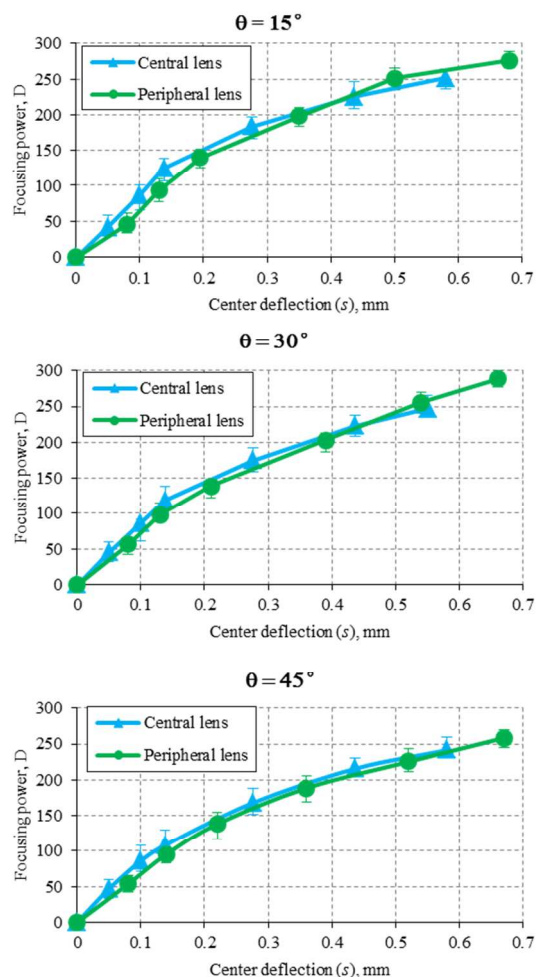
Fig. 5 Focusing power measurement while the big membrane was deformed. θ denotes the intersection angle between the optical axis of the peripheral lens and the vertical direction.

from about 0.76 mm at 240 µl to about 3.15 mm at 640 µl. While the big membrane was deformed, optical medium of about 60 µl was pumped into the top microfluidic network to highlight the position of individual single lenses. Fig. 4b shows the optical axes of the peripheral single lenses in the middle row of the array when the center deflection of the big membrane was 0, 0.76, 1.48, 2.1, 2.6, and 3.15 mm, respectively. At $h = 0$ mm, all the single lenses shared the same orientation. Their optical axes were therefore parallel. As the big membrane was deformed, the intersection angle between the optical axes of the peripheral single lenses in the same low with the center lens and the vertical direction (refers to θ and hereafter) changed from 0° to 45°, allowing for imaging at different angles.

Focusing power at various θ values

The effective focusing power of the single lenses was examined at different big membrane deformations ($\theta = 15°$, 30° and 45°) using fluorescence ray tracing (Fig. 5). As the big membrane deformed, in-plane strain was induced into the top surface of the big membrane and thus somewhat flattened the single lenses on the top. Therefore, additional fluid was needed to keep the focusing power unchanged. When $\theta > 0$, the focusing power of a peripheral lens was slightly greater than that of the center lens with the same big membrane deformation (as can be seen from Fig. 2b). This is due to the non-uniform strain field of the big membrane. In particular, the single lens in the center of the big membrane was subject to a higher strain magnitude than those in the peripheral region, and thus requires a higher differential pressure to deform. The focusing power difference does not affect the IHHE performance though because the device acquires images by temporal image integration and does not assume identical focusing powers of all the single lenses under a certain big membrane deformation. The results also showed that the focusing power of single lenses was not significantly affected by the θ value. In addition, the focusing powers of the center lens and of the peripheral lenses under the same center deflection were similar.
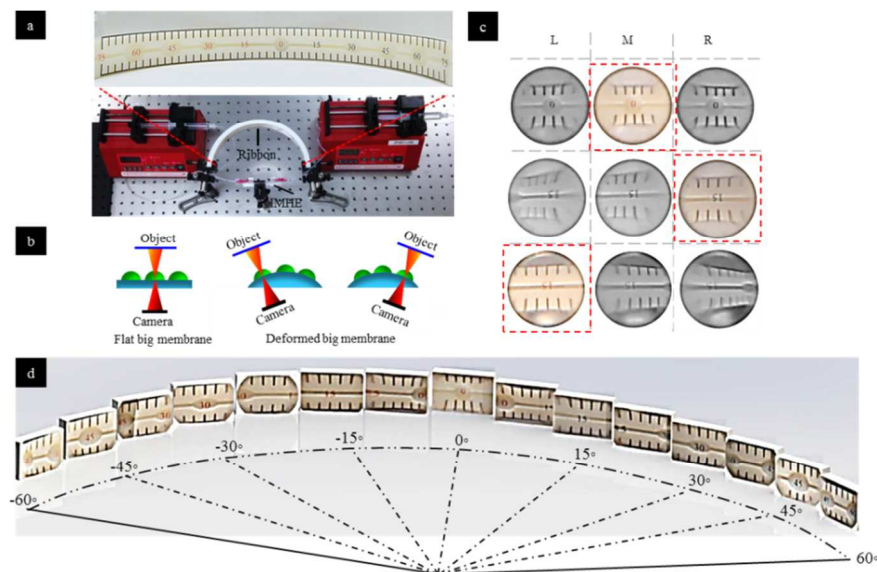

Fig. 6 Imaging with a large AOV. (a) Hemispherical ribbon marked with angles from negative 75° (in red) to positive 75° (in green). (b) Illustration of image acquisition. (c) Images viewed by the IHHE when the lens is upright and titled at +/-15°. Only the images in the highlighted boxes are used for assembling the final image in (d). (d) Images acquired at different AOVs (by tilting the lens from -52.5° to -52.5°) are collaged to show the overall AOV.

Imaging with a large AOV

The capability of the IHHE prototype of capturing images with a large AOV was demonstrated by observing characters printed on a semi-circular ribbon (Fig. 6a). The ribbon was 180 mm in diameter and printed by the 3D printer. The angles from –75° to +75° were indicated by lines with an increment of 3° and numbers with an increment of 15°. The IHHE prototype was positioned in the center of the semi-circular ribbon. Its position was adjusted to have the number '0' indicating 0° appear in the center lens. The CCD camera was placed behind the IHHE prototype, whose optical axis was always aligned to that of the single lens to be observed (Fig. 6b). The distance between the single lens and the camera was kept as 110 mm. The F-number of the camera (focal length/aperture) was kept constant at 5.0 during the entire measurement. At h=0 mm, the lens above the membrane center focused on the number '0' with the focusing power of about 30D. The AOV of each single lens was about 15°. The single lenses in the peripheral region and in the same row also saw the number '0', while the image appeared slightly off the center of field. At h=0.76 mm, the peripheral single lenses of both sides saw the number '15' (red on the left and green on the right), indicating an enlarged overall AOV (Fig. 6c). Similarly, the big membrane was further deformed to tilt the optical axes of peripheral single lenses to +/-7.5°, +/-22.5°, +/-30°, +/-37.5°, +/-45°, and +/-52.5°. The overall AOV was obtained after temporal integration of all these images. Given the current optical configuration, the overall AOV of up to about 120º was achieved (Fig. 6d).

Distinguishing objects at different depths and different angles

The adaptive focusing capability combined with the reconfigurable big membrane also allows the device to view objects at different depths and at different angles (Fig. 7). To validate this, two sets of letters were positioned spherically in front of the IHHE prototype: the letters of 'O', 'M' and 'U' in the first set encircled the IHHE from the left to the right at the angle of -30°, 0°, and +30° with the axis of the big membrane respectively. Each letter was at a distance of 32 mm from the center of the IHHE. Similarly, the letters 'B', 'S' and 'E' in the second set were positioned at the angle of -30°, 0°, and 30° with the optical axis of the big membrane respectively. Each letter was at a distance of 92 mm from the center of the IHHE.

The big membrane was first deflected to have the peripheral single lenses facing 30°, *i.e.* the left single lens oriented

Fig. 7: Adaptive focusing at varied viewing angles.

towards the letters of 'O' and 'B'; the middle single lens oriented towards the letters of 'M' and 'S'; and the right single lens oriented towards the letters of 'U' and 'E'. Afterwards, the letter 'B' was brought into focus by tuning the focusing power of the single lenses to about 50D. The focusing power was then increased to 100D to focus on the letter 'M', and tuned back to 50D to focus on letter 'E', completing the word of 'BME'. Similarly, the word of 'OSU' was viewed by tuning the focusing power of the single lenses to focus on individual letters (inset of Fig. 7). It is worth noting that when one letter was in focus, the other letter along the same line of sight was fairly blurred, indicating that the two letters at different depths can be well distinguished.

Discussions

Reconfigurable design with a small number of single lenses

The IHHE design arranges a fairly small number of membrane-enveloped fluidic lenses (a total of nine) with adaptive focusing powers on a flexible big membrane with a reconfigurable curvature. The aperture of each single lens is at least one order of magnitude greater than those in previous demonstrations of compound eye vision systems that have hundreds or even thousands of microscale single lenses. Given that the typical pixel size of CCD or CMOS sensors is on the order of tens of microns, the increased aperture size allows each single lens to capture images with a relatively high resolution. Subsequent imaging processing is thus simplified. However, different from conventional compound eyes where the orientations of adjacent single lenses only differentiate by a small angle no more than a few degrees, the differential orientation of adjacent single lenses in IHHE depends on the curvature of the big membrane. With a small curvature (the big membrane is nearly planar), the adjacent single lenses have a very small difference in their orientations. Their fields of view thus overlap with each other so that the entire field can be captured simultaneously. A large curvature is needed for increasing the AOV, which causes discrete fields of view with an un-covered region in between due to the increased differential angle between the adjacent single lenses. Therefore, the IHHE captures multiple images while the peripheral single lenses "*sweep*" the field during the big membrane deformation. In the meantime, single lenses are actuated to focus on the objects along their respective lines of sight.

Temporal image integration and the acquisition time

In the IHHE prototype, the final image with a large overall AOV is formed by joining multiple images with slightly overlapped fields of view, similar to stitched panorama. In particular, the objects in the overlapped areas of adjacent frames are used for correct stitching. However, since each image is acquired by a single lens with a different focusing power, individual images are not readily "*stitchable*". Proper magnification is needed to compensate the difference of focusing powers between adjacent single lenses before the images can be stitched. Moreover, parallax error may occur because the optical center of a peripheral lens shifts during big membrane deformation. The optimal strategy of stitching images is beyond the scope of this study and will be investigated in the future.

The total acquisition time depends on response time of the big membrane as well as that of single lenses, which are

determined by viscoelastic properties of the membrane material and the optical medium, and the actuation mechanism. Detailed analysis of the viscoelastic behaviour including the response time of such a system can be performed following the method reported in a previous publication[43]. Using a syringe pump as the actuation mechanism and glycerol/water mixture as the optical medium, the big membrane made of PDMS can be deformed from a planar surface to a dome shape with the center deflection of 3.15 mm within 3.6 seconds. Likewise, the small membrane can be deformed from a planar surface (0D) to a dome shape with the center deflection of 550 μm (275D) within 1.4 seconds. It is worth noting that the maximal flow rate of the syringe pump (500 ml/hr in this study) and the relatively long and distensible tubes used to connect to the syringe pump limit the response performance. This response time can be reduced by integrating an actuation mechanism within the IHHE device where external pumping and tubing are abolished, *e.g.* using an integrated electric or magnetic actuators[44-46].

Influence of the big membrane deformation on the focusing power of single lenses

As mentioned above, the non-uniform strain field on the top surface of the big membrane upon actuation may lead to focusing power difference among single lenses. Although this does not affect the IHHE performance, the non-uniform strain field may cause asymmetric deformation of the single lenses in the peripheral region and therefore optical aberration. Finite element analysis showed that the distortion of the single lens shape can be reduced by increasing the thickness ratio between the big membrane and the small membrane. Fig. 2b shows that with a thickness ratio of 4:1 as in the IHHE prototype, the asymmetric lens shape distortion caused by the big membrane deformation is negligible.

Possible integration with flexible photosensors

Since the images acquired by the single lenses on the deformed big membrane fall on a curved plane, conventional CCD or CMOS sensor on a planar surface is not adequate for image acquisition. To showcase the IHHE design with a low cost configuration, images were captured by placing a camera behind the IHHE device and having its lens plane perpendicular to the optical axis of the single lens of interest. For practical imaging applications, flexible photosensitive materials that deform with the elastomer substrates[12, 13, 15] can be positioned on the big membrane and aligned with each single lens. Such arrangement allows the use of air for big membrane actuation and may reduce the response time. Alternatively, elastomeric optical fibers/waveguides[47] may be used to transfer the light received by the single lenses to planar CCD or CMOS sensors. The strategies of integrating these technologies with adaptive fluidic lenses deserve future studies.

Limitations and possible solutions

The AOV of the IHHE prototype demonstrated in this study is lower than that in natural compound eye vision system, which often exceeds 150°. The AOV is determined by the distensibility of the big membrane and the bonding strength between the big membrane and the glass substrate. In this study, the big membrane did not rupture during the actuation. The delamination from the glass substrate was, however, observed when the actuation pressure was beyond 35 psi. This corresponded to a maximal θ value of about 54° and a maximal

AOV of 124° when the focusing power of single lenses was about 30D. The AOV can be further increased by increasing the bonding strength using other bonding methods, using thinner membranes and softer membrane materials, increasing the height of the chamber underneath the big membrane, or by increasing the focusing power of individual singles lenses.

A membrane-enveloped fluidic lens often suffers from optical aberration, as evidenced by the distorted image in its peripheral areas. This is caused by the deviation of the deformed profile of the membrane[48, 49] from an ideal spherical shape. The surface contours of deformed single lenses and of an ideal spherical lens were compared with the center deflections of 117 μm, 241 μm, 304 μm, and 550 μm. The results showed that the spherical deviation increased with the center deflection (data not shown) and may deteriorate the image quality at large deflections. As mentioned earlier, one solution of reducing such aberration is to have each single lens keep a small focusing power, sweep the field by actuating the big membrane, and collage the images. Alternatively, the spherical aberration of single lenses can be reduced by using a thickness-varied membrane whose deformation approximates a more spherical shape. Such membrane can be fabricated using previously reported methods[50]. The in-depth study of using such membranes in reducing spherical aberration will be reported in the future.

Conclusions

This work presents a unique configuration of adaptive optics that combines the structural characteristics of insect compound eye and human camera eye. This optical system was implemented on a bi-layered microfluidic device, where an array of deformable membrane-enveloped fluidic lenses within the top microfluidic layer achieves a tunable focusing power from 0D to 275D to mimic human camera eye, and an underlying elastomeric membrane in the bottom microfluidic layer can be reconfigurable to have varied curvatures. This allows spherical distribution of individual fluidic lenses in the top layer, similar to the arrangement in insect compound eyes. A tunable AOV as large as about 120° was demonstrated; and depth perception at varied angles was performed. While the device described here did not present an optimum in terms of imaging quality, the IHHE design clearly opens up a new avenue for adaptive optical systems with both the vari-focal capability and a large viewing angle in a compact setting.

Acknowledgements

Notes

a Laboratory for Biomedical Microsystems, Department of Biomedical Engineering, The Ohio State University, Columbus, OH, 43210 USA; Email: zhao.178@osu.edu

* To Whom All Correspondence Should Be Addressed.

References

1. A. Borst, *Curr. Biol.*, 2009, 19, R36-47.
2. E. K. Buschbeck and M. Friedrich, *Evolution: Education and Outreach*, 2008, 1, 448-462.

3. R. F. Chapman, *The insects: structure and function*, Cambridge university press, 1998.

4. P. T. Gonzalez-Bellido, T. J. Wardill and M. Juusola, *Proceedings of the National Academy of Sciences*, 2011, 108, 4224-4229.

5. R. Szema, J. Rastegar and L. Lee, *J Med Eng Technol*, 2004, 28, 117-124.

6. N. Franceschini, J.-M. Pichon, C. Blanes and J. Brady, *Philosophical Transactions of The Royal Society Of London. Series B: Biological Sciences*, 1992, 337, 283-294.

7. L. P. Lee and R. Szema, *Science*, 2005, 310, 1148-1150.

8. J. Duparre, P. Schreiber, P. Dannberg, T. Scharf, P. Pelli, R. Volkel, H. P. Herzig and A. Brauer, *Moems and Miniaturized Systems Iv*, 2004, 5346, 89-100.

9. K. H. Jeong, J. Kim and L. P. Lee, *Science*, 2006, 312, 557-561.

10. T. Wang, W. Yu, C. Li, H. Zhang, Z. Xu, Z. Lu and Q. Sun, *Opt Lett*, 2012, 37, 2397-2399.

11. L. Li and A. Y. Yi, *Opt Express*, 2010, 18, 18125-18137.

12. Y. M. Song, Y. Xie, V. Malyarchuk, J. Xiao, I. Jung, K. J. Choi, Z. Liu, H. Park, C. Lu, R. H. Kim, R. Li, K. B. Crozier, Y. Huang and J. A. Rogers, *Nature*, 2013, 497, 95-99.

13. I. Jung, J. Xiao, V. Malyarchuk, C. Lu, M. Li, Z. Liu, J. Yoon, Y. Huang and J. A. Rogers, *Proc Natl Acad Sci U S A*, 2011, 108, 1788-1793.

14. Q. He, J. Q. Liu, B. Yang, Y. Z. Dong and C. S. Yang, *Journal of Microelectromechanical Systems*, 2013, 22, 4-6.

15. H. C. Ko, M. P. Stoykovich, J. Song, V. Malyarchuk, W. M. Choi, C. J. Yu, J. B. Geddes, 3rd, J. Xiao, S. Wang, Y. Huang and J. A. Rogers, *Nature*, 2008, 454, 748-753.

16. B. G. Park, K. Choi, C. J. Jo and H. S. Lee, *Soft Matter*, 2012, 8, 1751-1755.

17. D. Floreano, R. Pericet-Camara, S. Viollet, F. Ruffier, A. Bruckner, R. Leitel, W. Buss, M. Menouni, F. Expert, R. Juston, M. K. Dobrzynski, G. L'Eplattenier, F. Recktenwald, H. A. Mallot and N. Franceschini, *Proceedings of the National Academy of Sciences of the United States of America*, 2013, 110, 9267-9272.

18. D. Keum, H. Jung and K. H. Jeong, *Small*, 2012, 8, 2169-2173.

19. P. Qu, F. Chen, H. Liu, Q. Yang, J. Lu, J. Si, Y. Wang and X. Hou, *Opt Express*, 2012, 20, 5775-5782.

20. Y. Kitamura, R. Shogenji, K. Yamada, S. Miyatake, M. Miyamoto, T. Morimoto, Y. Masaki, N. Kondou, D. Miyazaki and J. Tanida, *Applied Optics*, 2004, 43, 1719-1727.

21. W.-S. Chan, E. Y. Lam, M. K. Ng and G. Y. Mak, *Multidimensional Systems and Signal Processing*, 2007, 18, 83-101.

22. J. Duparré, P. Dannberg, P. Schreiber, A. Bräuer and A. Tünnermann, *Applied Optics*, 2005, 44, 2949-2956.

23. A. Brückner, J. Duparré, R. Leitel, P. Dannberg, A. Bräuer and A. Tünnermann, *Optics express*, 2010, 18, 24379-24394.

24. J. Howard and A. Snyder, *Proceedings of the Royal Society of London. Series B. Biological Sciences*, 1983, 217, 287-307.

25. M. P. Keating and P. Geometric, Butterworth Heinemann, Boston, 2002.

26. M. F. Land and D.-E. Nilsson, *Animal eyes*, Oxford University Press, 2012.

27. W. Song, A. E. Vasdekis and D. Psaltis, *Lab on a chip*, 2012, 12, 3590-3597.

28. W. Song and D. Psaltis, *Lab on a Chip*, 2013, 13, 2708-2713.

29. Y. Yang, L. Chin, J. Tsai, D. Tsai, N. Zheludev and A. Liu, *Lab on a Chip*, 2012, 12, 3785-3790.

30. D. Psaltis, S. R. Quake and C. Yang, *Nature*, 2006, 442, 381-386.

31. Y. Zhao, Z. S. Stratton, F. Guo, M. I. Lapsley, C. Y. Chan, S.-C. S. Lin and T. J. Huang, *Lab on a Chip*, 2013, 13, 17-24.

32. N.-T. Nguyen, *Biomicrofluidics*, 2010, 4, 031501.

33. Y. Seow, A. Liu, L. Chin, X. Li, H. Huang, T. Cheng and X. Zhou, *Applied Physics Letters*, 2008, 93, 084101.

34. J. Shi, Z. Stratton, S.-C. S. Lin, H. Huang and T. J. Huang, *Microfluidics and Nanofluidics*, 2010, 9, 313-318.

35. Y. Seow, S. Lim and H. Lee, *Lab on a Chip*, 2012, 12, 3810-3815.

36. X. Mao, S.-C. S. Lin, M. I. Lapsley, J. Shi, B. K. Juluri and T. J. Huang, *Lab on a Chip*, 2009, 9, 2050-2058.

37. C. Zhao, Y. Liu, Y. Zhao, N. Fang and T. J. Huang, *Nature communications*, 2013, 4.

38. L. Dong, A. K. Agarwal, D. J. Beebe and H. Jiang, *Nature*, 2006, 442, 551-554.

39. B. Berge, 2005.

40. W. Zhang, K. Aljasem, H. Zappe and A. Seifert, *Optics express*, 2011, 19, 2347-2362.

41. P. Fei, Z. He, C. Zheng, T. Chen, Y. Men and Y. Huang, *Lab on a Chip*, 2011, 11, 2835-2841.

42. H. Ren and S.-T. Wu, *Introduction to adaptive lenses*, Wiley, Hoboken, N.J., 2012.

43. Q. Wang, X. Zhang and Y. Zhao, *Sensors and Actuators B: Chemical*, 2014.

44. S. W. Lee and S. S. Lee, *Applied physics letters*, 2007, 90, 121129.

45. S. T. Choi, J. Y. Lee, J. O. Kwon, S. Lee and W. Kim, *Optics letters*, 2011, 36, 1920-1922.

46. K. Wei, N. W. Domicone and Y. Zhao, *Optics Letters*, 2014, 39, 1318-1321.

47. J. Kim, Google Patents, 2013.

48. Q. Yang, P. Kobrin, C. Seabury, S. Narayanaswamy and W. Christian, *Applied optics*, 2008, 47, 3658-3668.

49. S. T. Choi, B. S. Son, G. W. Seo, S.-Y. Park and K.-S. Lee, *Optics Express*, 2014, 22, 6133-6146.

50. Q. Wang and Y. Zhao, in *Proceeding of 15th International Conference on Miniaturized Systems for Chemistry and Life Sciences* Seattle, WA, 2011, pp. 1113-1115.